

## **Hydraulic fracturing: Laboratory evidence of the brittle-to-ductile transition with depth**

Runhua Feng<sup>1\*</sup>, Shuo Liu<sup>1</sup>, Joel Sarout<sup>2</sup>, Jeremie Dautriat<sup>2</sup>, Zhiqi Zhong<sup>1,3</sup>, Reza Rezaee<sup>1</sup>,  
Mohammad Sarmadivaleh<sup>1\*</sup>

<sup>1</sup>School of WASM: Minerals, Energy and Chemical Engineering, Curtin University, 26 Dick Perry Ave, Kensington, WA 6151 Australia

<sup>2</sup>CSIRO Energy, Perth, WA 6151, Australia

<sup>3</sup>College of Energy, Chengdu University of Technology, Chengdu, China

\*Corresponding author:

E-mail address: runhua.feng@student.curtin.edu.au (R.Feng);  
mohammad.sarmadivaleh@curtin.edu.au (M.Sarmadivaleh)

### **Highlights:**

- Hydraulic fracturing experiments are conducted on artificial materials exhibiting a wide range of rheology subjected to true triaxial stresses with a low ( $\sigma_v = 6.5$  MPa,  $\sigma_H = 3$  MPa, and  $\sigma_h = 1.5$  MPa), and a higher (15 MPa, 10 MPa, and 5 MPa) confinement; the wellbore pressure, three dimensional (3D) and volumetric strain induced by hydraulic fracturing are interpreted.
- The intermediate stress plays a profound role in hydraulic fracture (HF) propagation subjected to normal faulting regime, i.e., the transition of intermediate strain are temporally observed from brittle to ductile samples.
- The orientation angle of hydraulic fracture is highly inclined to the maximum horizontal  $\sigma_H$  (or vertical  $\sigma_v$ ) stresses in brittle/semi-brittle samples; in contrast, the angle is reduced in semi-ductile samples, and nearly reaches to zero (parallel to  $\sigma_H$  and  $\sigma_v$ ) for ductile samples.
- The fracturing area are shown to be reduced as the decrease of brittleness for either low or higher confinement; the tortuosity and roughness of fracture surface increases as the confinement.

## Abstract

Understanding the propagation of hydraulic fracture (HF) is essential for effectively stimulating the hydrocarbon production of unconventional reservoirs. Hydraulic fracturing may induce distinct failure modes within the formation, depending on the rheology of the solid and the *in-situ* stresses. A brittle-to-ductile transition of HF is thus anticipated with increasing depth, although only scarce data are available to support this hypothesis. Here we carry out laboratory hydraulic fracturing experiments in artificial geomaterials exhibiting a wide range of rheology: cubic samples 50x50x50 mm<sup>3</sup> in size are subjected to true triaxial stresses with either a low ( $\sigma_v = 6.5$  MPa,  $\sigma_H = 3$  MPa, and  $\sigma_h = 1.5$  MPa), or a higher (15 MPa, 10 MPa, and 5 MPa) confinement. The 3D strains induced by hydraulic fracturing are monitored and interpreted; and X-ray Computed Tomography (CT) imaging is used to document the HF geometry. Finally, a correlation between the normalized fracture area ( $A_{FN}$ ) and the brittleness index (BI) of tested samples is introduced. Our results reveal that: (i) The intermediate stress plays a profound role in hydraulic fracture propagation subjected to the normal faulting regimes (i.e., the transitional intermediate strain observed from brittle to ductile samples); (ii) The orientation angle of hydraulic fracture is highly inclined to the maximum horizontal  $\sigma_H$  (or vertical  $\sigma_v$ ) stresses in brittle/semi-brittle samples; as BI decreases, the angle inclination is reduced for that of semi-ductile samples, finally reaches to zero (parallel to  $\sigma_H$  and  $\sigma_v$ ) in ductile sample. (iii) The normalized fracturing area ( $A_{FN}$ ) decreases as the decrease of BI among different samples under either low or higher confinement. Interestingly, for the same type of sample, the tortuosity and roughness of fracture surface leads to a larger surface area of hydraulic fracture at the higher confinement rather than that of low confinement. This study reveals the importance of understanding the underground brittle-to-ductile behaviour of hydraulic fracture prior to the field implementation.

## 1. Introduction

The deformation of geo-materials incorporate the process as shear stress is increased toward failure: I- initial elastic deformation; II – non-recoverable deformation, i.e., brittle micro-cracking, or ductile/plastic flow; III – micro-cracks nucleation and macroscopic fracture propagation. The three stages are highly influenced by the confinement of stress, a brittle-to-ductile transitional failure is thus expected and observed as the increase of confinement (Aharonov and Scholz 2019; Evans et al. 1990; Minaeian 2014; Nygård et al. 2006; Vachaparampil and Ghassemi 2017; Wong and Baud 2012; Zhang et al. 1993). However, much fewer studies focus on the transitional deformation induced by hydraulic fracturing emerging

in a wide range of underground engineering applications. Hydro-mechanical force is the main driven mechanism for the propagation of hydraulic fracture and with the same analogy, such transitional failure is expected as the function of confinement. Deeply understanding this transitional deformation can facilitate not only theoretical/numerical modelling but also provide critical insights for field applications associated with hydraulic fracturing.

When hydraulic fracture initiates and propagates within geo-materials under *in-situ* stresses, three types of failure modes are often observed: mode-I (tensile), mode-II (shear), and mixed-mode-I and II (Economides and Nolte 1989; Gischig and Preisig 2015; Wu 2006). The stress anisotropy, fluid mechanics, natural fractures, and rock mechanical properties are recognized as the most influential factors in the failure mode (Gischig and Preisig 2015; Li et al. 2020; Liu et al. 2020; Papanastasiou 1997; Sarmadivaleh 2012; Wang 2019; Wang et al. 2013; Yang et al. 2021; Zeng et al. 2020; Zhang et al. 2009; Zhou et al. 2008). Incorporating all these parameters in fracturing analysis is complicated to be achieved. Since the hydraulic fracture growth is a dynamic process where the damage is mainly accumulated adjacent to the tip within the process zone (Desroches et al. 1994; Elices et al. 2002; Garagash 2019; Ju et al. 2021; Liu and Lecampion 2021; Papanastasiou 1997), which allows an alternative way studying the fracturing process. Several studies demonstrated that the plastic yielding/stress softening at the tip will absorb the effective injection energy, which significantly hinders the fracture propagation and results in a uniformed fracture geometry in ductile rocks (Feng et al. 2020; Ju et al. 2021; Papanastasiou 1997; Parisio et al. 2021).

Recently, Ju et al. (2021) performed a 3D numerical model for hydraulic fracture propagation in tightly brittle and ductile reservoirs. They confirmed that the stress concentration near the fracture tip is highly accommodated in the ductile reservoir. Parisio et al. (2021) carried out an experimental study of the brittle-to-ductile transition of hydraulic fracture within Polymethyl Methacrylate (PMMA). They observed complex fracture patterns under non-uniform stress distribution in the sample under the brittle regime. The complexity of fracture is significantly reduced as the ductility is increased. These studies revealed that a brittle-to-ductile transition is anticipated for the hydraulic fracture in a wide range of rocks types in elevated confinements. However, such experimental study on a wide range of geo-materials is still lacking, which is essential to provide the data set required for the calibration of the modelling suitable for field applications.

In this paper, we present hydro-mechanical data based on hydraulic fracturing tests on variable types of geomaterials subjected to two sets of true triaxial stress conditions (TTSC), i.e., low confining ( $\sigma_1=6.5\text{MPa}$ ,  $\sigma_2=3\text{MPa}$ , and  $\sigma_3=1.5\text{MPa}$ ), and higher confining stresses ( $\sigma_1=15\text{MPa}$ ,  $\sigma_2=10\text{MPa}$ , and  $\sigma_3=5\text{MPa}$ ); the evolution of wellbore pressure and the three mutually orthogonal strains induced by hydraulic fracture propagation are interpreted. We also interpreted the geometry and surface area ( $A_F$ ) of hydraulic fracture based on the visualisation of the X-ray Computational Tomography (CT) images of tested samples. These quantifications allow us to correlate the  $A_F$  and the brittleness index (BI) of the samples subjected to hydraulic fracturing; this correlation is compared against the previous numerical study.

### 3. Experimental Procedure

The six types of samples (see details of sample preparation and rock characterization in **Appendix A**) are used for hydraulic fracturing experiments under true triaxial stress conditions. Honey is used as fracturing fluid due to its Newtonian behavior. A micro-metering needle valve  $V_i$  is added to the injection inlet to restrict the flow rate when the rock breakdown takes place (Bunger 2005; Sarmadivaleh 2012). The experiments consist of three main components (**a**-pumping system; **b**-fracturing system **c**-data acquisition system) and are conducted in the following steps (**Fig.2**):

- (i) The cubic samples are initially loaded into the cell (**Fig.2b**), where the injection tube glued into the wellbore is connected to the injection line of the fracturing fluid.
- (ii) The confining stresses are simultaneously elevated to a target value (at low confining case of  $\sigma_v = 6.5 \text{ MPa}$  (940psi),  $\sigma_H = 3 \text{ MPa}$  (440psi),  $\sigma_h = 1.5 \text{ MPa}$  (220psi) or the higher case of  $\sigma_v = 15 \text{ MPa}$  (2175psi),  $\sigma_H = 10 \text{ MPa}$  (1450psi),  $\sigma_h = 5 \text{ MPa}$  (725psi)): all stresses elevated to minimum stress, then two bigger stresses raised to the intermediate level, finally, the maximum stress is reached on one side, i.e., the loading rate is sufficiently small and constant to avoid any premature cracks induced by stresses. Waiting for at least 12hrs to ensure the stresses reach an equilibrium state, which also allows the time-dependent deformation (creep) has been fully developed prior to the initiation and propagation of the hydraulic fracture.
- (iii) Vacuuming the injection line before injecting the honey into the wellbore (**Fig.2a**); monitoring the wellbore pressure for 1 hr when it reached a constant vacuum pressure value of -14 psi.

- (iv) Start to inject the fracturing fluid into wellbore; start to monitor the wellbore pressure and 3D strain at the same time.

After the fracturing tests are completed, all samples are scanned a 3D X-ray Computed Tomography (XCT) images at a voxel resolution of 0.1 x 0.1 x 0.1 mm (Siemens SOMATOM Definition AS, set for helical scanning at 140 kV/500 mA) (Liu et al. 2022) were produced to document the geometry of hydraulic fractures within the samples. All quantities from CT images are interpreted by Avizo software.

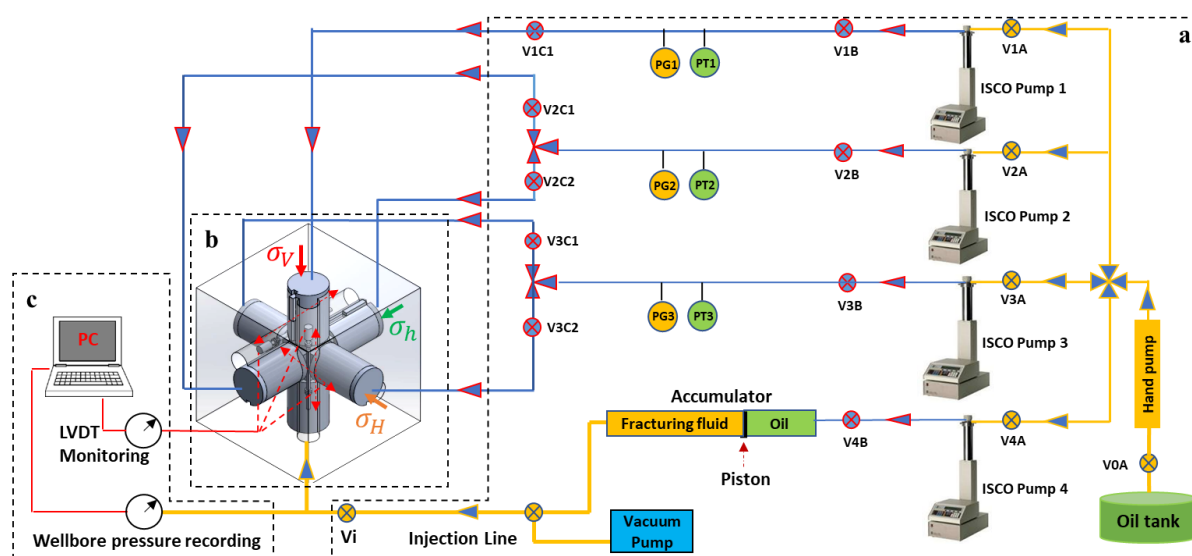


**Fig.2** Schematic of hydraulic fracturing experimental setup: **a** Pumping system; **b** fracturing system; and **c** data acquisition system. *PT* pressure transducer, *PG* pressure gauge, *V* valve, *V<sub>i</sub>* micro-meter valve, *LVDT* Linear Variable Differential Transformer, *PC* data acquisition.

## 4. Results

The representative hydro-mechanical results for tested samples ( $S_1$ - $S_6$ ) under low and high confinement are presented in **Section 4.1**; We also discuss the characteristics of intermediate strain ( $\epsilon_H$ ) induced by hydraulic fracture propagation (**Section 4.2**). Moreover, the geometry of hydraulic fracture under both confinement are presented (**Section 4.3**). Finally, the correlation between fractured area and brittleness index (BI) is reported in **Section 4.4**. According to the quantification of brittleness index (BI) (Feng et al (2022)) and the failure characteristics of samples subjected to triaxial compression tests (**Figs.A2 and A3**), the six types of samples are classified into: brittle PMMA (BI=0.97), semi-brittle quartz-rich  $S_1$  (BI=0.68), semi-brittle mixed-average  $S_4$  (BI=0.57), semi-ductile calcite-rich  $S_3$  (BI=0.44), the ductile clay-rich  $S_5$  (BI=0.38) and clay-rich  $S_2$  (BI=0.35) under the low confinement. The same classification with

This is a non-peer reviewed EarthArXiv preprint.

different BI values under higher confinement: PMMA (BI=0.94), S<sub>1</sub> (BI=0.35), S<sub>4</sub> (BI=0.26), S<sub>3</sub> (BI=0.24), S<sub>5</sub> (BI=0.14), and S<sub>2</sub> (BI=0.09).

#### 4.1 Hydro-mechanical data

**Figs.3** and **4** show the representative hydro-mechanical data (i.e., the wellbore pressure and 3D strain (volumetric) induced by hydraulic fracturing) subjected to low (**Fig.3**) and high (**Fig.4**) confinement for the different samples: brittle PMMA (**Fig.3a and 4a**), semi-brittle S<sub>1</sub> (**Fig.3b and 4b**), semi-brittle S<sub>4</sub> (**Fig.3c and 4c**), semi-ductile S<sub>3</sub> (**Fig.3d and 4d**), ductile S<sub>5</sub> (**Fig.3e and 4e**), and S<sub>2</sub> (**Fig.3f and 4f**). The variation of 3D strain prior to the breakdown (maximum) pressure remains constant comparing to the strain after the breakdown pressure. The minimum horizontal strain  $\varepsilon_h$  is mainly produced by the propagation of fracture (negative  $\varepsilon_h$  in green curve), whereas the positive vertical strain  $\varepsilon_v$  (blue) indicates the vertical compression induced by the vertical stress. For brittle PMMA, and semi-brittle rock S<sub>1</sub>, the strain  $\varepsilon_h$  abruptly increases after the (breakdown pressure) (**Figs.3 and 4a and b**); in contrast, for the ductile rock (S<sub>5</sub> and S<sub>2</sub>), the  $\varepsilon_h$  are gradually increased to the peak value (**Figs.3 and 4e and f**).

Interestingly, the magnitude of strain  $\varepsilon_H$  along the intermediate horizontal stress  $\sigma_H$  (orange curve) shows a slightly negative deflection (tension) for semi-brittle sample S<sub>1</sub> under both low (**Fig.3b**) and high confinement (**Fig.4b**); a slightly positive deflection (compression) for ductile sample S<sub>2</sub> under low confinement (**Fig.3f**) but a significantly positive deflection (compression) of  $\varepsilon_H$  is observed for S<sub>2</sub> under high confinement (**Fig.4f**). The more specific characteristics of intermediate strain  $\varepsilon_H$  will be discussed in **Sections 4.2 and 5.2**. Another important observation is the coincidence of the intermediate ( $\varepsilon_H$ ) and vertical ( $\varepsilon_v$ ) strain for semi-ductile S<sub>3</sub> (**Fig.4d**), ductile S<sub>5</sub> (**Fig.4e**) and S<sub>2</sub> (**Fig.4f**) subjected to the high confinement, which would be discussed in **Section 5**.

The volumetric strains ( $\varepsilon_T$ ) are correspondingly shown at top right corner (purple curve) for each test. Under the low confinement (**Figs.3**): i) for brittle PMMA (**Figs.3a**), and semi-brittle sample S<sub>1</sub>(**Figs.3b**), the volumetric strain  $\varepsilon_T$  are abruptly increased to the maximum value (negative deflection) after the period of constancy, indicating a significant dilated behaviour; ii) for semi-brittle samples S<sub>4</sub> (**Figs.3c**), and semi-ductile sample S<sub>3</sub> (**Figs.3d**), the  $\varepsilon_T$  are more gradually developed (nonlinear dilated behaviour); iii) whereas for the ductile sample S<sub>5</sub> (**Figs.3e**) the  $\varepsilon_T$  keeps relatively constant from the initiation to the end of propagation; notably for ductile sample S<sub>2</sub> (**Figs.3f**), the positive deflection of  $\varepsilon_T$  indicates a compressive manner of the deformation subjected to hydraulic fracturing.

This is a non-peer reviewed EarthArXiv preprint.

Under the high confinement (**Figs.4**): i) for brittle PMMA (**Figs.4a**), the volumetric strain  $\varepsilon_T$  shows a more significant negative deflection (relatively linear after the breakdown) comparing to that under the low confinement; for semi-brittle sample S<sub>1</sub>, the  $\varepsilon_T$  shows a significant negative deflection with strong nonlinearity (**Figs.4b**). ii) for semi-brittle S<sub>4</sub> (**Figs.4c**), semi-ductile S<sub>3</sub> (**Figs.4d**), and ductile samples S<sub>5</sub> (**Figs.4e**), the  $\varepsilon_T$  exhibits the analogous slightly negative deflection; ii) while for ductile sample S<sub>2</sub>, volumetric strain  $\varepsilon_T$  is relatively constant from the early initiation until the end of propagation.

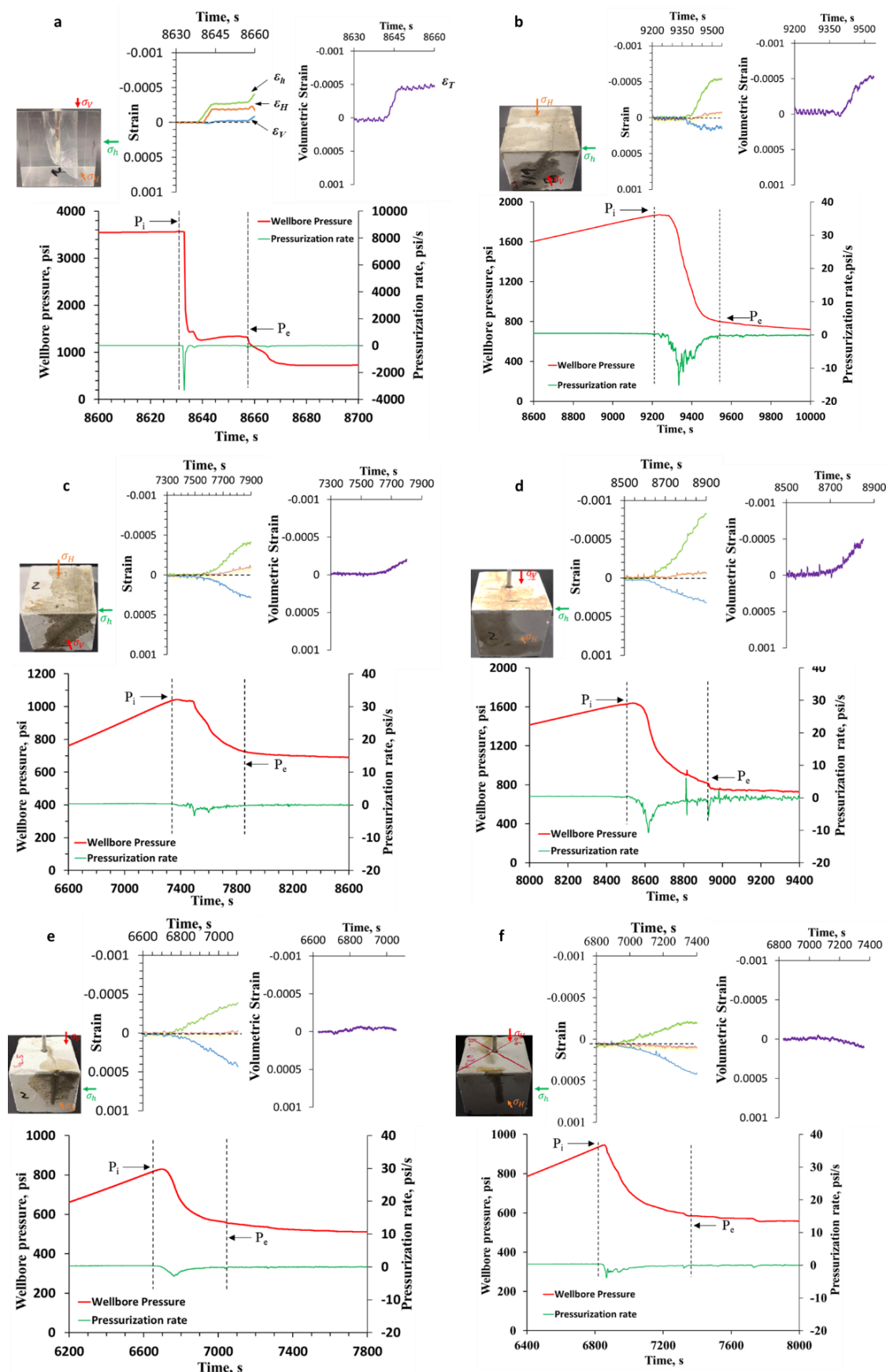


**Fig.3** Synchronization of wellbore pressure and hydraulic fracture induced strain (vertical- $\epsilon_v$ , maximum horizontal (intermediate)- $\epsilon_H$ , and minimum horizontal- $\epsilon_h$ ) under low confinement (6.5MPa , 3MPa, and 1.5MPa): a) PMMA2 b) S<sub>1</sub> c) S<sub>4</sub> d) S<sub>3</sub> e) S<sub>5</sub> f) S<sub>2</sub>.  $P_i$  and  $P_e$  denote the borehole pressure at the initiation



and at the end of fracture propagation, respectively. The corresponding each sample after test are shown at the left. The volumetric strain ( $\epsilon_v$ ) are shown at the top-right.

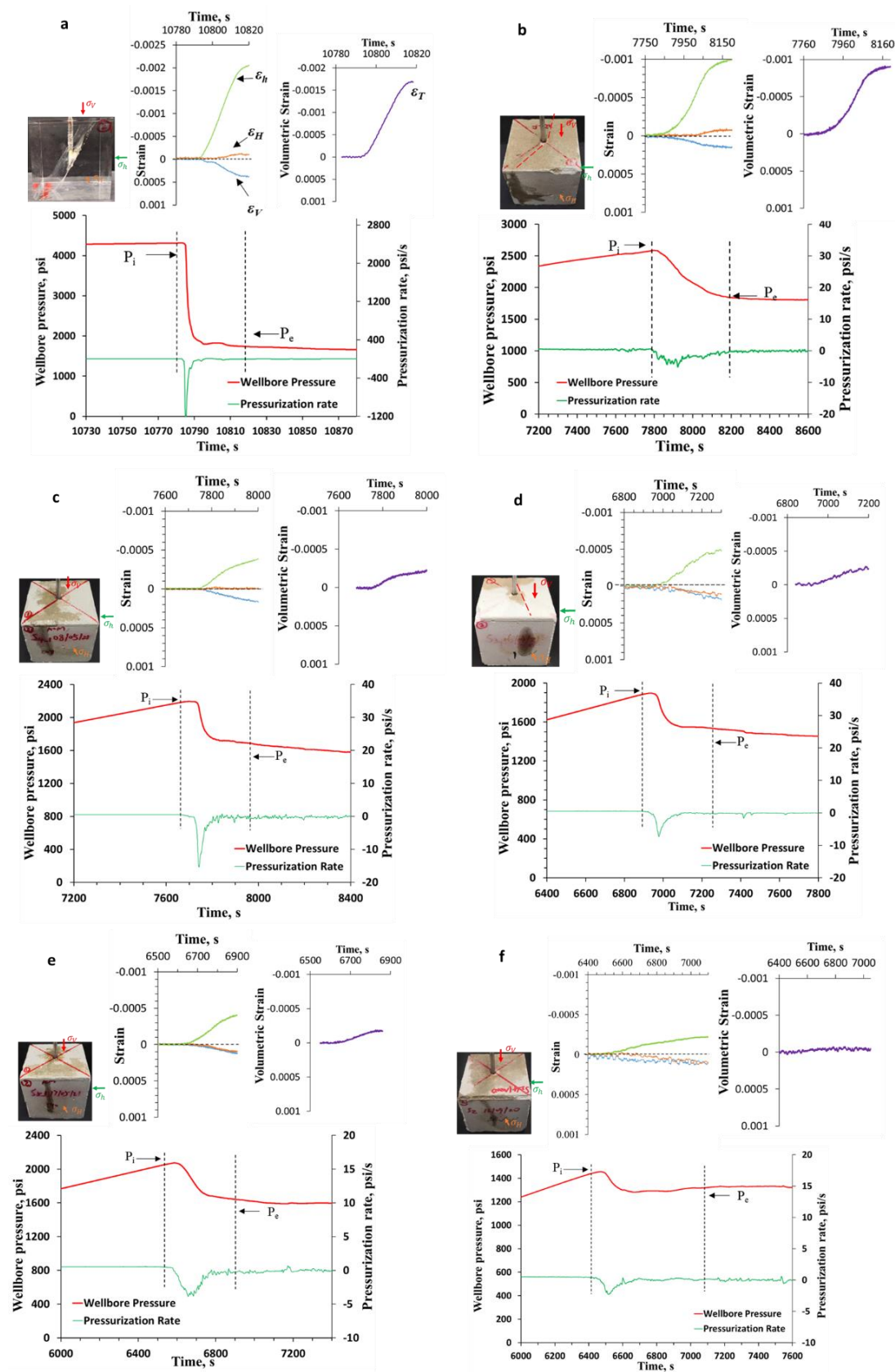


**Fig.4** Synchronization of wellbore pressure and hydraulic fracture induced strain (vertical- $\epsilon_v$ , maximum horizontal (intermediate)- $\epsilon_H$ , and minimum horizontal- $\epsilon_h$ ) under high confinement (15MPa , 10MPa,

and 5MPa): a) PMMA4 b) S<sub>1</sub> c) S<sub>4</sub> d) S<sub>3</sub> e) S<sub>5</sub> f) S<sub>2</sub>. P<sub>i</sub> and P<sub>e</sub> denote the borehole pressure at the initiation and at the end of fracture propagation, respectively. The corresponding each sample after test are shown at the left. The volumetric strain ( $\epsilon_v$ ) are shown at the top-right.

#### 4.2 Intermediate strain ( $\epsilon_H$ ) transition

Refer to the hydro-mechanical data set (**Figs.3 and 4**), the vertical strain  $\epsilon_v$  shows a compression, and the minimum horizontal strain  $\epsilon_h$  exhibits tension after breakdown pressure reaches for all samples. However, the characteristics of intermediate strain  $\epsilon_H$  are highly variable, depending on the sample types and confinement (**Fig.5**). For semi-ductile S<sub>3</sub>, and ductile samples S<sub>5</sub> and S<sub>2</sub> under higher confinement (**Fig.5b**), the magnitude of  $\epsilon_H$  is significantly larger than that of lower confinement (**Fig.5a**). In summary, the significant transitions of  $\epsilon_H$  from the brittle to ductile samples are observed:

Under the low confinement (**Fig.5a**): the intermediate strain  $\epsilon_H$  shows a significant tensile deflection for brittle PMMA; a moderate tensile deflection for semi-brittle rock sample S<sub>1</sub> and S<sub>4</sub>; a slight deflection for semi-ductile S<sub>3</sub>; a nearly constant  $\epsilon_H$  for ductile S<sub>5</sub>; while a slight compressive deflection for ductile rock sample S<sub>2</sub>. For the high confinement (**Fig.5b**), the transition is analogous to the lower one: the negative deflection of  $\epsilon_H$  becomes ease for PMMA, and still exhibits the highest value among all samples; for the rock samples (from S<sub>1</sub> to S<sub>5</sub>), the moderate negative deflection of  $\epsilon_H$  are observed in semi-brittle rock sample S<sub>1</sub> and S<sub>4</sub>, but a significant positive compression of  $\epsilon_H$  are found in semi-ductile S<sub>3</sub>, ductile S<sub>5</sub> and S<sub>2</sub>.

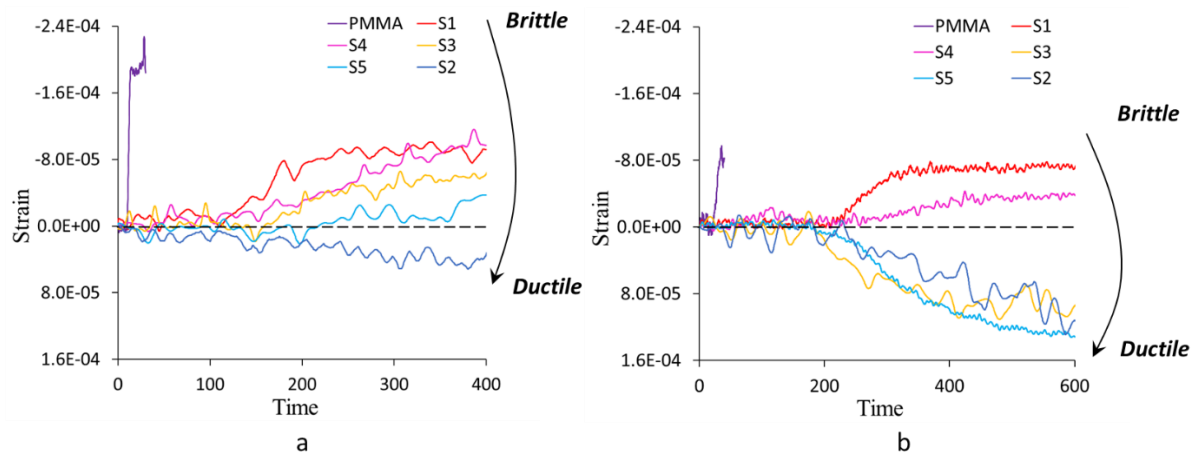


**Fig.5** Transition of intermediate strain  $\epsilon_H$  from brittle to ductile samples for a) low confinement b) high confinement

#### 4.3 Geometry of Hydraulic Fracture

The geometry of hydraulic fracture for different samples subjected to low confinement (i.e., 6.5, 3, and 1.5MPa) are shown in **Fig.6**. The fractures are highly tilted with respect to both  $\sigma_H$  and  $\sigma_h$  for brittle PMMA (**Fig.6a**), and semi-brittle rock S<sub>1</sub> (**Fig.6b**) and S<sub>4</sub> (**Fig.6c**). For the

semi-ductile  $S_3$ (**Fig.6d**) and ductile rock  $S_5$  (**Fig.6e**), the tilted angle are significantly reduced. In contrast, for ductile sample  $S_2$  the fractures are nearly orthogonal to  $\sigma_h$  only (**Fig.6f**). Overall, it turns out a clear transition from highly tilted (brittle) to orthogonal (ductile) fractures as the increase of ductility. This analogous phenomenon is also observed in the samples subjected to higher confinement (i.e., 15, 10, and 5MPa) (**Fig.7**). The most interesting observation is the significant shear failure induced by hydraulic fracturing within PMMA: the geometry of hydraulic fracture (HF) is highly tilted to  $\varepsilon_V$  and  $\varepsilon_h$  (**Fig.7a**), instead of inclining to  $\varepsilon_H$  and  $\varepsilon_h$  subjected to the lower confinement. Macroscopically, the geometry of hydraulic fractures are more planar/smooth under high confinement (**Fig.7**) rather than that of relatively tortuous fractures under the low confinement (**Fig.6**).

The experimental geometry of hydraulic fracture(HF) with respect to the brittle and ductile rocks (**Figs.6 and 7**) are in good agreement with the numerical study performed by Ju et al. (2021): for brittle reservoir the fracture is severely tilted and result in a nonplanar geometry (**Fig.8a**), while for the ductile reservoir the inclination of fracture is highly mitigated due to the tip plasticity (**Fig.8c**), resulting in an axisymmetrically short fracture. Their numerical results are shown to be more consistent with our experimental geometry of HF subjected to the high confinement (**Fig.7**).

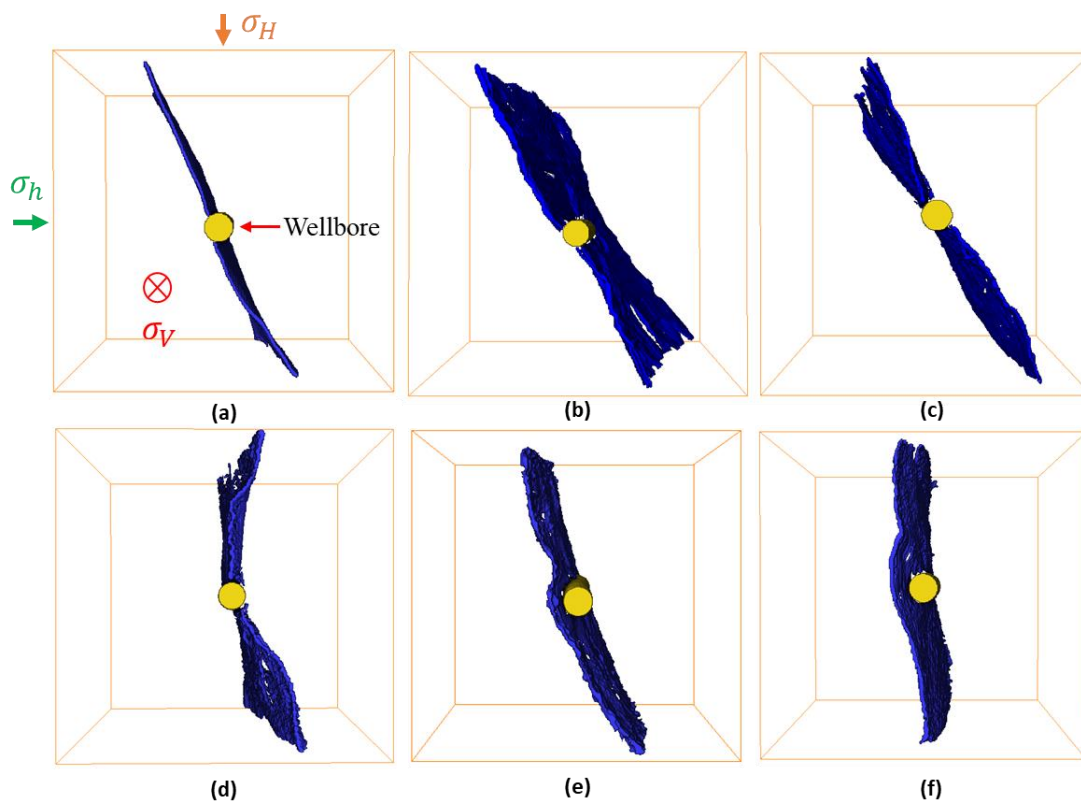


**Fig.6.** Geometry of hydraulic fracture from brittle to ductile transition a) PMMA b) S<sub>1</sub> c) S<sub>4</sub> d) S<sub>3</sub> e) S<sub>5</sub> f) S<sub>2</sub> under 6.5, 3.0, 1.5MPa

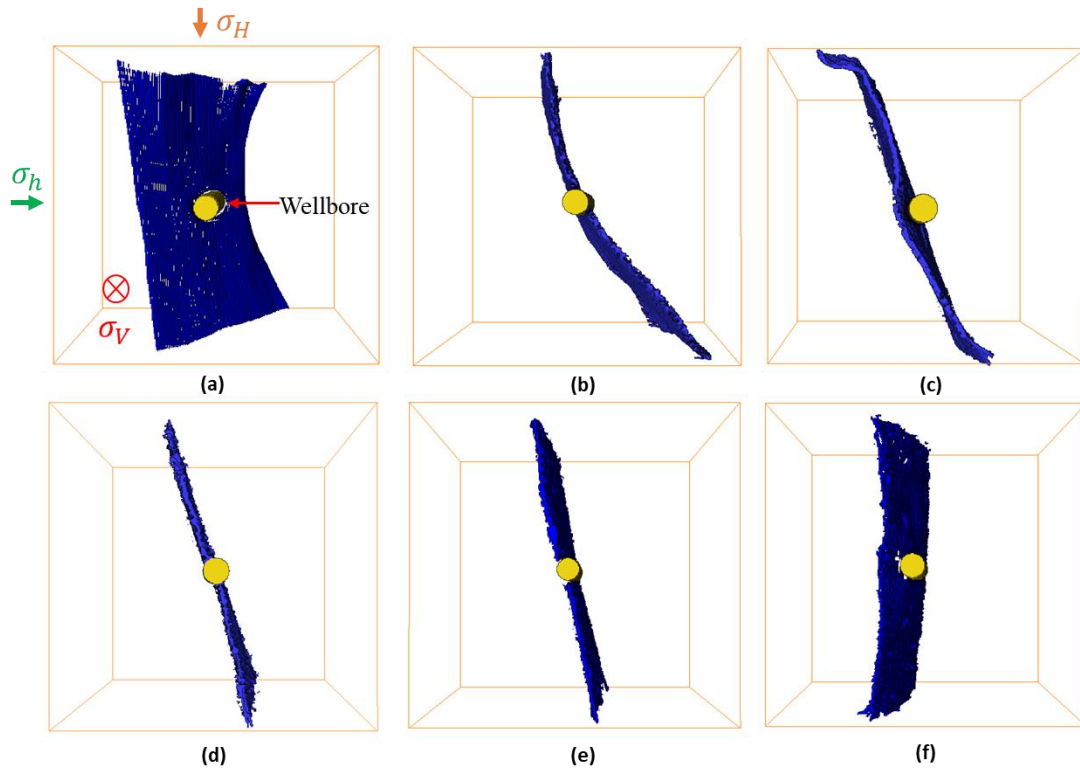


**Fig.7.** Geometry of hydraulic fracture from brittle to ductile transition a) PMMA b) S<sub>1</sub> c) S<sub>4</sub> d) S<sub>3</sub> e) S<sub>5</sub> f) S<sub>2</sub> under 15, 10, 5MPa

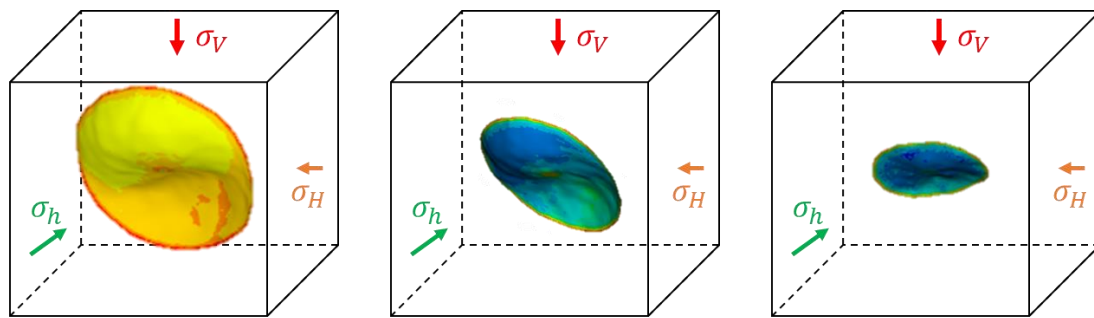


**Fig.8.** Numerical modelling of the morphology of hydraulic fracture from a) brittle, b) semi-brittle, and c) ductile reservoir under true triaxial stresses  $\sigma_v=30\text{MPa}$ ,  $\sigma_H=\sigma_h=20\text{MPa}$ . Images modified from a 3D numerical work (Ju et al. (2021)).

#### 4.4 Fractured area verse BI

Ju et al. (2021) numerically studied the relation between fractured area and the brittleness index (BI) of shale reservoir. He showed that the fractured area is increased as the increase of BI. Here we quantify the hydraulic fractured area based on the CT images of tested rock samples (S<sub>1</sub> to S<sub>5</sub>). We normalized the numerical ( $A_{TN}$ ) and experimental fractured area ( $A_{FN}$ ) based

on the sample dimension, and plot both  $A_{TN}$  and  $A_{FN}$  verse BI (**Fig.9**). Both  $A_{TN}$  and  $A_{FN}$  show an increased trend as the increase of BI. Notably, under the lower confinement, the fitting of  $A_{FN}$  and BI shows a second polynomial relation (negative coefficient). On the other hand, under the high confinement, the analogous second polynomial relation (positive coefficients) are observed for both  $A_{FN}$  and  $A_{TN}$  verse BI; but their quantities are significantly different.

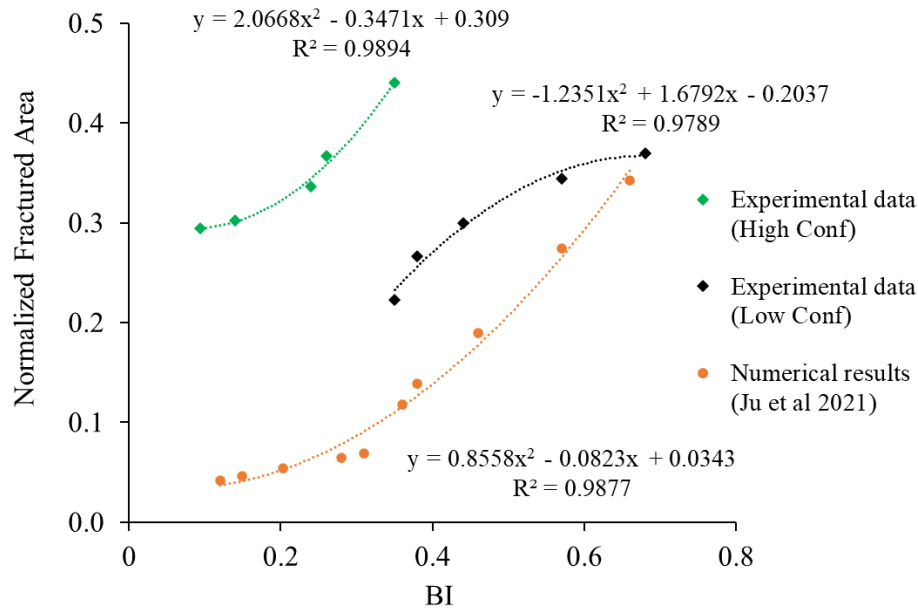


**Fig.9** Normalized fractured area vs brittleness index (BI) based on our experimental results and literature data

## 5. Discussion and implementations

### 5.1 Deformation characteristics

The characteristics of hydro-mechanical deformation can be indicated by the 3D strain (vertical- $\epsilon_v$ , intermediate- $\epsilon_H$ , and minimum horizontal- $\epsilon_h$ ), and the volumetric strain ( $\epsilon_T$ ). Under the lower confinement, for brittle PMMA (**Fig.3a**), and semi-brittle samples  $S_1$  (**Fig.3b**) the volumetric strain and small portion of axial strain indicate the fracture deformation are relatively localized. On the other hand, for semi-brittle  $S_4$  (**Fig.3c**), and semi-ductile  $S_3$  (**Fig.3d**) the volumetric strain ( $\epsilon_T$ ) experiences more nonlinearity; while for ductile samples  $S_5$  (**Fig.3e**) and  $S_2$  (**Fig.3f**), the relative constant or compressive  $\epsilon_T$  reveal that nonlocalized (spatially extended) plastic deformation are expected to be developed during the fracture propagation within the sample. Under the higher confinement, the failure of PMMA(**Fig.4a**) is dominated by vertical shear dilation (PMMA), while for semi-brittle rock  $S_1$  (**Fig.4b**) the lateral shear-tensile opening is dominated; the more pronounced strain is attributed to higher breakdown/net

pressure. In contrast to the significantly dilated volumetric strain ( $\epsilon_T$ ) observed for PMMA and  $S_1$ , the volume of the samples are only slightly dilated for semi-brittle  $S_4$  (**Fig.4c**), semi-ductile  $S_3$  (**Fig.4d**), and ductile sample  $S_5$  (**Fig.4e**); while it stay relatively constant for ductile sample  $S_2$  (**Fig.4f**). These observations indicate that the plastic deformation are highly nonlocalized within semi-ductile  $S_3$ , and ductile samples ( $S_5$  and  $S_2$ ) where the compression of intermediate ( $\epsilon_H$ ) and vertical strain ( $\epsilon_V$ ) are highly coincided (**Figs.4d,e, and f**). Such evidence of nonlocalized (spatially extended) plastic deformation induced by fracture propagation (stress/hydraulic) are also observed and proven in the numerical/experimental studies (Brantut et al. 2011; Huang and Chen 2021; Huang and Ghassemi 2016; Liu and Brantut 2022; Parisio et al. 2021; Ramos Gurjao et al. 2022; Richard et al. 2021; Schmidt et al. 2022; Tan et al. 2021; Vinci et al. 2014; Wrobel et al. 2022; Zhang et al. 2020).

## 5.2 Role of intermediate stress ( $\sigma_H$ ) in hydraulic fracture

The intermediate stress  $\sigma_H$  is considered as an important parameter for the stress intensity factor ( $K_{HF}$ ) if the geometry of hydraulic fracture (HF) is inclined to directions of both horizontal stresses (**Eqs.B6 to B8**), which is often observed in the laboratory or field (Sarvaramini et al. 2019; Yu et al. 2022). The previous studies demonstrated the significant role of  $\sigma_H$  in the mechanical properties, and associated failure modes induced by the elevated mechanical stresses on sandstone and shale (Minaeian 2014). In this study, the intermediate strain  $\epsilon_H$  induced by the coupled hydraulic and mechanical force are highly variable regarding the sample types, and the confinement. The deflection of  $\epsilon_H$  exhibits a clear brittle-to-ductile transition among the tested samples especially for the higher confining case (**Fig.5**). Noteworthy, for semi-ductile and ductile samples subjected to the higher confinement, the  $\epsilon_H$  are significantly compressive after the early initiation stage (i.e., 200s), then starts to coincident with the vertical strain ( $\epsilon_V$ ) (**Figs.4d,e and f**). This observation can be explained by the more pronounced nonlocal (spatial extend) deformation induced by hydraulic fracture in the semi-ductile/ductile samples subjected to higher confining stresses (as discussed in **Section 5.1**).

## 5.3 Geometry of hydraulic fracture

The representative transitional geometry of hydraulic fracture (HF) for brittle and ductile samples (**Figs.6 and 7**) are in good agreement with the numerical study (**Fig.8**) performed by Ju et al. (2021). **Fig.10** shows a typical shear failure induced by true tri-axial stresses compression (TTSC) i.e.,  $\sigma_v > \sigma_H > \sigma_h$  (Minaeian 2014; Rahjoo and Eberhardt 2021). Prior to this failure, a fictitious weak plane (normal faulting regime) is anticipated within the sample

subjected to the stresses (**Fig.10**). Noteworthy, this fictitious plane is distinct from the weakest plane for propagation of a hydraulic fracture (i.e., the one perpendicular to minimum horizontal stress). Based on the geometry observed in our tested samples (**Figs.6 and 7**), the representative schematic of brittle to ductile transition for the hydraulic fracture subjected to the designed stress regime are displayed in **Fig.10**.

Under the higher confinement: for HF initiates and reaches to breakdown pressure within brittle PMMA, due to the extremely high stress concentration near the crack tip, the highly effective propagation energy converted from pressurized fracturing fluid (higher  $K_I (P_f)$  in **Eq.B7**) causes the fracture propagating highly along to the normal faulting regime (see **Fig.10, Fig.11a, and Fig.4a**), without being significantly affected by the stress redistribution. For semi-brittle rocks  $S_1$  and  $S_4$ , the high stress concentration near the fracture tip is mitigated due to the strain softening ( $K_I (\sigma_{coh})$  in **Eq.B7**), causing the vertical shearing failure appears to be highly eased (**Fig.11b**), instead, the hydraulic fracture is inclined to intermediate stress  $\sigma_H$  due to stress redistribution. Subjected to low confinement, the alleviation of stress concentration near tip is also observed in the PMMA, in which the geometry of HF is analogous to the semi-brittle rocks  $S_1$  and  $S_4$ .

Moreover, for semi-ductile sample ( $S_3$ ), and ductile rocks ( $S_5$  and  $S_2$ ) subjected to the higher confinement: (i) the significant tip plasticity and softening behaviour (Feng et al. 2020; Ju et al. 2021; Papanastasiou 1997) highly reduce the stress concentration, which significantly reduces the kinematic energy transformation from the accumulated injection energy (lower  $K_{HF}$ ). (ii) The reduction of effective propagation energy allow the stress redistributed on the samples. These mechanisms explain the geometry of hydraulic fracture always propagated along the weakest plane in semi-ductile/ductile samples, i.e., nearly perpendicular to the minimum horizontal stress (**Fig.11c or d**), without being significantly affected by the fictitious weak plane induced by the deviatoric stress state ( $\sigma_V > \sigma_H > \sigma_h$ ) shown in **Fig.10**. Notably, for the rock-like materials ( $S_1$  to  $S_5$ ), the macroscopic geometry of hydraulic fractures subjected to high confinement (**Fig.7**) are more planar than that of low confinement (**Fig.6**), which is attributed to the higher confinement/ductility stabilizing the fracture propagation (lower  $K_{HF}$  in **Eq.B6**).

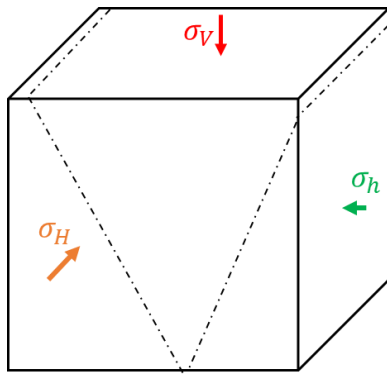


**Fig.10** The failure mode of brittle materials under true triaxial stress compression i.e.,  $\sigma_v > \sigma_H > \sigma_h$  (Minaeian 2014; Rahjoo and Eberhardt 2021).

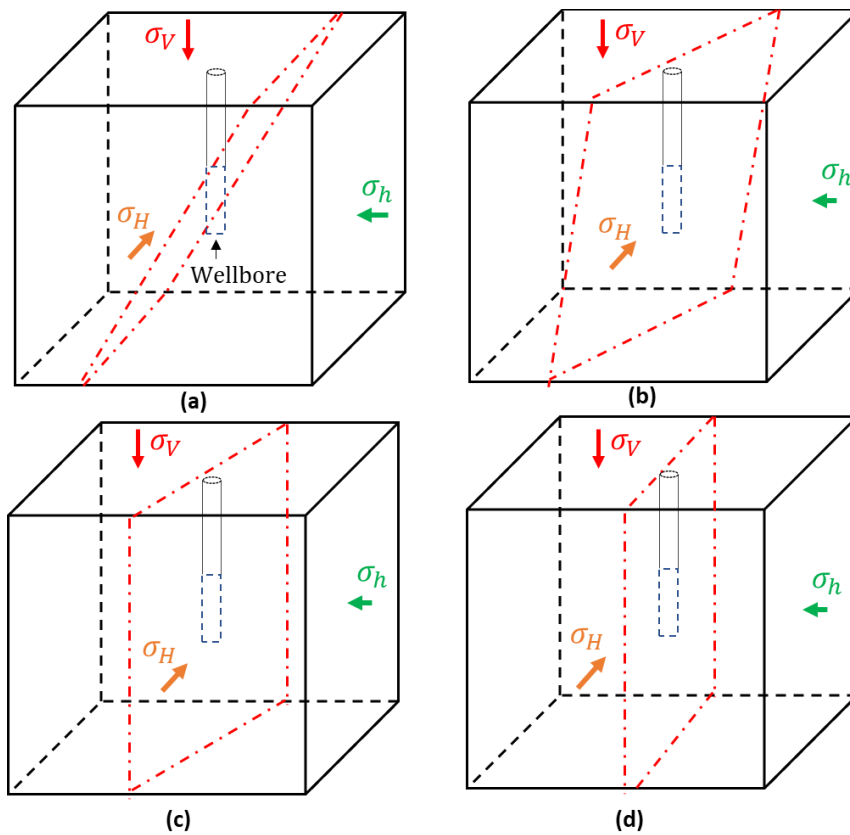


**Fig.11** Representative Geometry of hydraulic fracture from brittle to ductile transition: **a)** brittle PMMA (under high confinement) **b)** brittle PMMA (under low confinement) or brittle/semi-brittle sample **c)** semi-brittle/semi-ductile sample **d)** ductile sample. Note: the failure plane shown above is a simplified diagram, not necessarily indicating the fracture will exactly follow that plane or penetrated to the boundary of sample.

#### 5.4 Role of BI in Fractured area

laboratory results indicated that the fractured area ( $A_{FN}$ ) are reduced from brittle to ductile samples subjected to both low and high confinement (**Fig.9**), which is in good agreement with



the numerical study recently performed by Ju et al. (2021). As shown in **Fig.9**, the experimental results subjected to the high confinement ( $A_{FN}$  verse BI) shows an analogous polynomial relation comparing to the numerical results ( $A_{TN}$  verse BI); regardless of their quantities. For laboratory experiments, the limited sample size and continuously injected energy allow the fluid-driven fractures penetrate the boundary of sample; while the HF are retained within the boundary of numerical model due to the early termination of fracture propagation in ductile reservoirs (Ju et al. 2021).

Interestingly, for the same type of tested sample, the fractured area ( $A_{FN}$ ) subjected to high confinement (15MPa, 10 MPa, and 5MPa) are larger than that of lower confinement (6.5MPa, 3 MPa, and 1.5MPa) (**Fig.9**), although the brittleness index (BI) of former one is reduced. This could be attributed to: (i) higher deviatoric horizontal stress exerted on the samples subjected to high confinement (Van Dam and De Pater 1999; Van Dam et al. 2000). (ii) higher stress concentration near the fracture tip due to the higher breakdown/propagation pressure. This coupled mechanism causes the fracture propagate in a manner of relatively higher effective stress and sufficient propagating time, resulting in a more tortuous fracture with relatively rougher surface in the view of meso-scale (**Fig.12**).

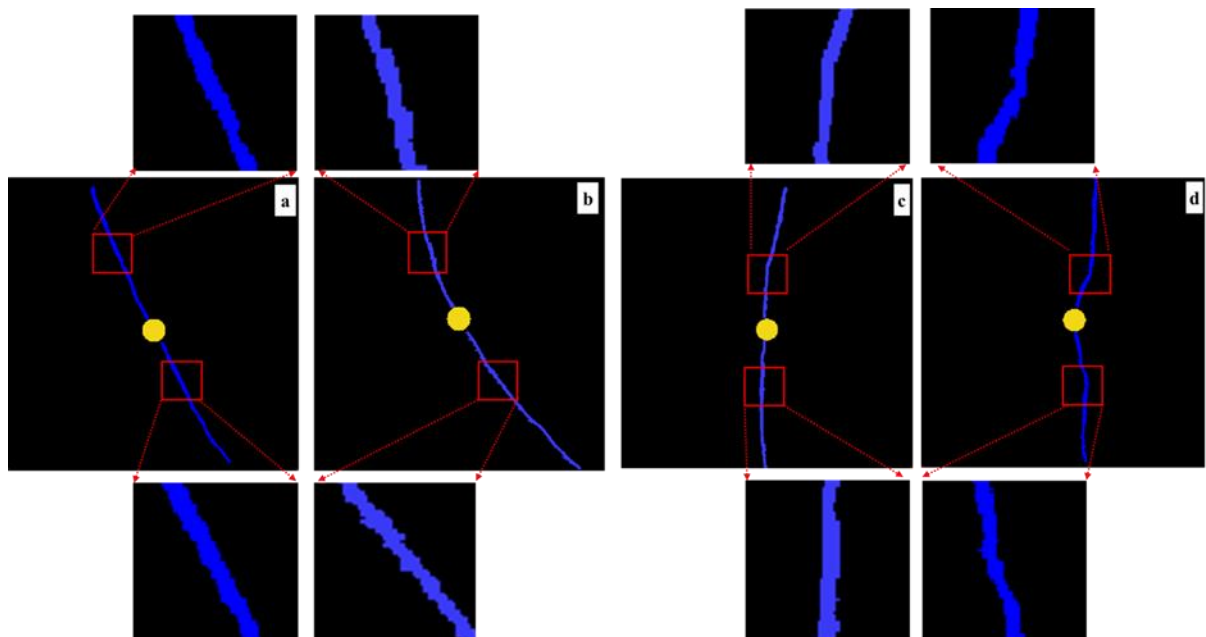


**Fig.12** CT images of hydraulic fracture in semi-brittle rock  $S_1$  under a) low and a) high confinement; ductile rock  $S_2$  under c) low and d) high confinement

## 6. Conclusion

The initiation and propagation of hydraulic fractures in geomaterials plays an important role in geology (Weinberg and Regenauer-Lieb 2010), reservoir stimulation (Bakhshi et al. 2021;

Huang and Chen 2021; Mandal et al. 2020), and the management of micro-seismicity (Amitrano 2003). However, the brittle-to-ductile transition of hydraulic fracturing process with depth has been rarely quantified in the laboratory despite its pivotal role for benchmarking field operations.

In this study, we conducted hydraulic fracturing experiments on five types of rock samples in addition to PMMA, which represents the extreme brittle reference. The samples were subjected to true triaxial stress conditions (TTSC), and during fluid injection wellbore pressure and the three-dimensional (3D) strains induced by hydraulic fracture propagation were simultaneously monitored. After each experiment the fractured sample was imaged using X-ray Computed Tomography (XCT); the 3D images were used to quantitatively evaluate the morphology and area of the induced hydraulic fracture (Avizo software). These experiments are designed to shed light on the hydraulic fracturing response as a function of depth for a wide range of engineering applications. The following conclusions are addressed based on this study:

- (i) The interpretation of the hydro-mechanical data (3D strain and volumetric strain ( $\epsilon_T$ )) reveals the distinctive deformation characteristics for the brittle/semi-brittle, semi-ductile, and ductile samples. The non-localized (spatial extend) plastic deformation induced by hydraulic fracturing is pronounced in a semi-ductile sample (e.g.,  $S_3$ ), and a ductile sample (e.g.,  $S_5$  and  $S_2$ ), especially for the higher confinement (**Figs.3 and 4**). In contrast, the fracture deformation is more localized dilation for the brittle PMMA (**Figs.3a and b**), and the semi-brittle sample  $S_1$  (**Figs.4a and b**).
- (ii) The intermediate stress ( $\sigma_H$ ) may play a profound role in HF propagation and associated rock deformation: for the tested samples subjected to normal faulting regime (i.e.,  $\sigma_v > \sigma_H > \sigma_h$ ), the intermediate strain  $\epsilon_H$  transits from tensile deflection to positive compression from the brittle to ductile samples; this phenomenon is enhanced as the increase of confinement (**Fig.5**).
- (iii) The high-to-low inclined angle for hydraulic fractures (HFs) are observed from the brittle/semi-brittle to semi-ductile/ductile samples (**Figs.6 and 7**): For the brittle PMMA under the high confinement, extremely high stress concentration near the crack tip leads to a strong hydro-shearing fracture (**Figs.7a and 11a**), which is consistent with the normal faulting regime (**Fig.10**). For the semi-brittle samples ( $S_1$  and  $S_4$ ), the nonlocalized plasticity reduces the stress concentration near the fracture tip, inhibiting vertical hydro-shearing failure, instead, the horizontal hydro-dilating fractures are formed (see **Figs.7b and c; Figs.11b and c**). While for the semi-ductile sample  $S_3$  and

the ductile samples ( $S_5$  and  $S_2$ ), the significantly nonlocalized plasticity reduces the near-tip stress concentration, which significantly reduces the effective propagation energy (Feng et al. 2020; Ju et al. 2021; Papanastasiou 1997; Parisio et al. 2021), allowing stress redistribution within the ductile rock surrounding the tip. This mechanism is thought to be the cause of the highly mitigated inclination of hydraulic fractures observed in samples  $S_3$  (**Figs.6d and 7d; Fig.11c**) and  $S_5$  (**Figs.6e and 7e; Fig.11c**), which contrasts with the fracture induced in sample  $S_2$ , i.e., nearly perpendicular to the minimum horizontal stress (**Figs.6f and 7f; Fig.11d**).

- (iv) The measured surface area of the hydraulic fractures is reduced when transiting from the brittle to the ductile regime, regardless of the confinement (**Fig 11**), which is in good agreement with the numerical study reported by Ju et al. (2021). Notably, for the same type of sample under high confinement (15MPa, 10 MPa, and 5MPa), the fractured area ( $A_{FN}$ ) is shown to be larger than that for lower confinement values (6.5MPa, 3 MPa, and 1.5MPa), despite the fact that the brittleness index (BI) is reduced when confinement is significantly higher. This is attributed to a more tortuous fracture with a relatively rougher surface at high confinement (**Fig 12**).

### **Declaration of competing interest**

The authors declare that they have no known competing interest

### **Acknowledgments**

The first author sincerely thanks China Scholarship Council- Curtin International Postgraduate Research Scholarship (CSC-CIPRS, Grant No. 201808190001) for their financial support on this research.

### **Appendix A: Test Materials and Mechanical properties**

Synthetic rock blocks constituted of variable fractions of fine-grain quartz, kaolinite clay, calcite, and Standard Portland cement mixture (**Table A1**) are moulded. The PMMA were additionally used as an ideally homogeneous and brittle reference. More details on the fabrication procedures of block samples can be found in Sarmadivaleh and Rasouli (2015) and Feng et al. (2020). The prepared cubic/cylindrical blocks and the schematic of cubic sample assembly for a typical hydraulic fracturing test are shown in **Fig.A1**. In field, defects and stress concentrations play a role in hydraulic fracture propagating in mix-modes, i.e., non-perpendicular to the minimum principal stress (Parisio et al. 2021). To allow the stress concentration generating around the borehole, we design for drilling a 2/3 depth of the borehole

(Feng et al. 2020; Parisio et al. 2021) (**Fig.A1**). The mechanical properties of prepared blocks are shown in **Table A2**. Details of the procedures for UCS and TCS testing used to determine these values can be found in Feng et al. (2020).

The physical photo of five new types of samples after Tri-axial compressive tests (TCS) are presented in **Fig.A2**. The shear failure is observed in Quartz-rich  $S_1$  (**Fig.A2a**), Average-mix  $S_4$  (**Fig.A2b**) and Calcite-rich  $S_3$  (**Fig.A2c**) samples, while for the two types of Clay-rich sample  $S_5$  (**Fig.A2d**) and  $S_2$  (**Fig.A2e**) there are no significant failure plane due to their high ductility under 3.4MPa of confinement. The representative stress-strain curve from TCS is shown in **Fig.A3**, in which the higher portion of plastic strain (axial/lateral) are observed in both clay-rich samples ( $S_2$  and  $S_5$ ).

**Table A1.** Composition and density of the five synthetic rock formulations (mineral cement mixtures) used in this study.

Mineral-cement mixture	Silica (%)	Kaolinite (%)	Calcite (%)	Cement (%)	Density(g/cm <sup>3</sup> )
Quartz-rich( $S_1$ )	52.5%	22.5%	0.0%	25%	1.58
Clay-rich( $S_2$ )	22.5%	52.5%	0.0%	25%	1.26
Calcite-rich( $S_3$ )	15.0%	7.5%	52.5%	25%	1.44
Mixed average( $S_4$ )	30.0%	22.5%	22.5%	25%	1.50
Clay-rich <sub>2</sub> ( $S_5$ )	30.0%	45%	0.0%	25%	1.46

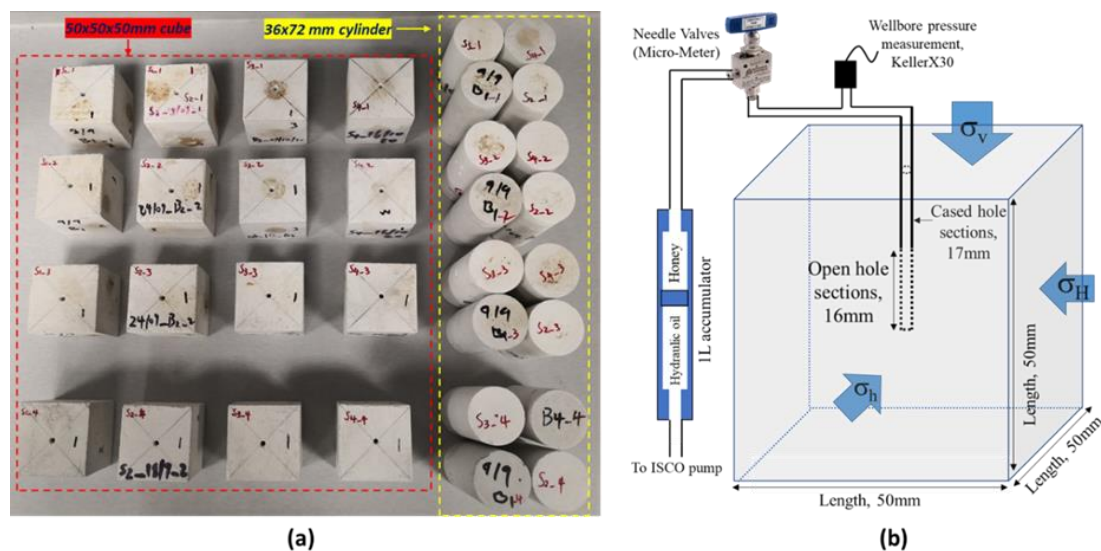


**Fig.A1** a) Part of the synthetic rock samples used in this study: a) 50x50x50mm cubes for hydraulic fracturing, and 36x72mm cylindrical plugs for mechanical characterisation; b) schematic of a typical cubic sample prepared for hydraulic fracturing tests (modified from Feng et al. (2022)).

**Table A2.** Mechanical properties of the mineral-cement mixtures and PMMA used in this study, and determined through unconfined (UCS) and triaxial (TCS) compression tests.

Mineral-cement mixture	Young's modulus $E$ (GPa)	Poisson's ratio $\nu$ (-)	Friction angle $\Phi$ ( $^{\circ}$ )	Cohesion $C_0$ (MPa)	P-wave velocity $V_p$ (km/s)	S-wave velocity $V_s$ (km/s)	Porosity $\phi$ (-)
Quartz-rich( $S_1$ )	6.9*	0.17*	42*	1.76*	2.1	1.4	0.29
Clay-rich( $S_2$ )	2.6*	0.1*	35.3*	0.6*	1.3	0.87	0.3
Calcite-rich( $S_3$ )	3.2*	0.21*	40.9*	0.9*	1.69	1.07	0.2
Mixed average( $S_4$ )	3.0*	0.18*	35.8*	1.5*	1.8	1.17	0.24
Clay-rich2( $S_5$ )	1.6*	0.17*	37.3*	0.8*	1.47	0.97	0.3
PMMA( $S_6$ )	6.2**	0.39**	14.4**	44.6**	2.75	1.4	0

\* UCS tests are conducted on dry samples, and TCS tests are conducted in dry conditions at 0.6, 2.1, and 3.4 MPa confining pressure.

\*\* Data reported in the literature.

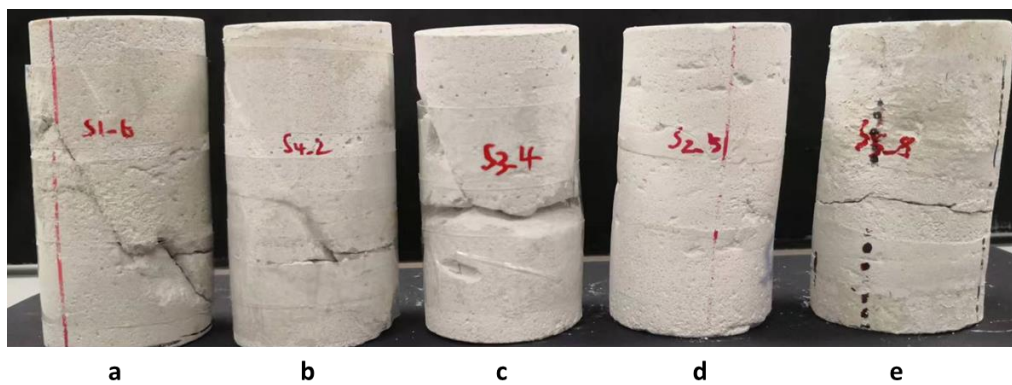


**Fig.A2** Failure patterns of the five new synthetic samples after TCS under confinement of 3.4MPa: a) Quartz-rich  $S_1$  b) Average-mix  $S_4$  c) Calcite-rich  $S_3$  d) Clay-rich  $S_2$  e) Clay-rich  $S_5$

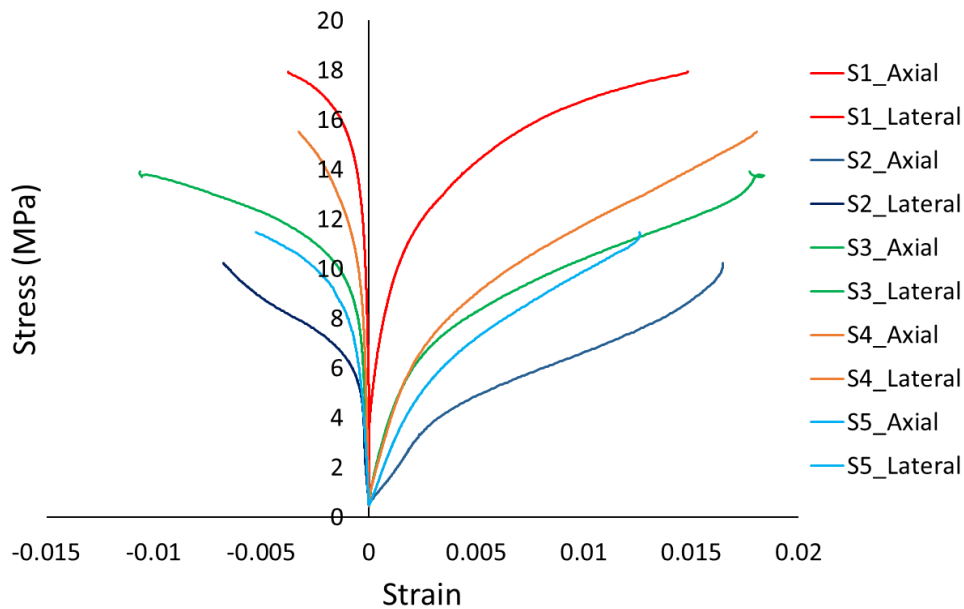


**Fig.A3** Stress vs strain curve obtained from TCS testing on samples ( $S_1$  to  $S_5$ )

## Appendix B. Propagation Criterion for Hydraulic Fracture

Stress intensity factor ( $K$ ) at the crack tip has been studied as an important parameter in linear elastic fracture mechanics (Irwin 1957). Later, Barenblatt (1962) and Dugdale (1960) proposed a well-known Barenblatt-Dugdale model, accounting for the nonlinear material behaviour into a small size of cohesive zone near the crack tip. Hillerborg et al. (1976) introduced a model for the finite cohesive zone, adapting to the propagation of a cohesive crack in elastic material when the tensile softening takes place (Boone et al. 1986; Desroches et al. 1994; Papanastasiou and Thiercelin 1993).

For propagating a penny-shaped hydraulic fracture (**Fig.B1**), the three aspects- (i) fluid pressure, (ii) *in-situ* stresses, and (iii) cohesive stresses are necessarily considered into the stress intensity factor ( $K_{HF}$ ) (Lhomme 2005). The pressurized fracturing fluid provides a positive contribution to the stress intensity factor  $K_I(P_f)$  reads:

$$K_I(P_f) = 2 \sqrt{\frac{R}{\pi}} \int_0^{c_f} K_{np}(\xi, c) p_f(\xi, t) d\xi \quad (\text{B1})$$

Where  $P_f$  is the fluid pressure,  $R$  is the radius of fracture extent,  $R_f$  is the radius of fluid front (**Fig.C1**);  $\xi = x/R_w$ ,  $c = R/R_w$ , and  $c_f = R_f/R_w$  are the normalized length variables to borehole radius  $R_w$ ; the kernel function  $K_{np}(\xi, c)$  denotes the effect of wellbore geometry in stress intensity factor (Keer et al. 1977; Lhomme 2005; Nilson and Proffer 1984).

If we consider a hydraulic fracture subjected to the both horizontal stresses, i.e., minimum ( $\sigma_h$ ) and intermediate ( $\sigma_H$ ), the resultant normal stress on the fracture walls ( $\sigma_r$ ) negatively contributed to the stress intensity factor  $K_I(\sigma_r)$  reads:

$$K_I(\sigma_r) = -2 \sqrt{\frac{R}{\pi}} \sigma_r \int_0^c K_{np}(\xi, c) d\xi \quad (\text{B2})$$

The inelastic behaviour can be modelled by tensile cohesive stresses exerted on the fracture wall within the cohesive zone (Elices et al. 2002; Garagash 2019; Lhomme 2005; Liu and Lecampion 2021), a degradation function  $f_{wct}$  is introduced to address the linear/nonlinear relation between the cohesive stress ( $\sigma_{coh}$ ) and associated fracture opening ( $w$ ) from the peak load to critical fracture opening ( $w_c$ ):

$$\sigma_{coh} = \sigma_t f_{wct}, \quad 0 < f_{wct} < 1, \quad w < w_c \quad (\text{B3})$$

$$\sigma_{coh} = 0, \quad w \geq w_c \quad (\text{B4})$$

This is a non-peer reviewed EarthArXiv preprint.

The cohesive stresses provided a negative contribution to the stress intensity factor  $K_I(\sigma_{coh})$  reads as:

$$K_I(\sigma_{coh}) = -2 \sqrt{\frac{R}{\pi}} \sigma_t \int_{c_v}^c K_{np}(\xi, c) f_{w_{ct}} d\xi \quad (\text{B5})$$

Where  $R_v$  is the visible radius of the crack (**Fig.B1**);  $c_v = (R_v - R_w) / R_w$

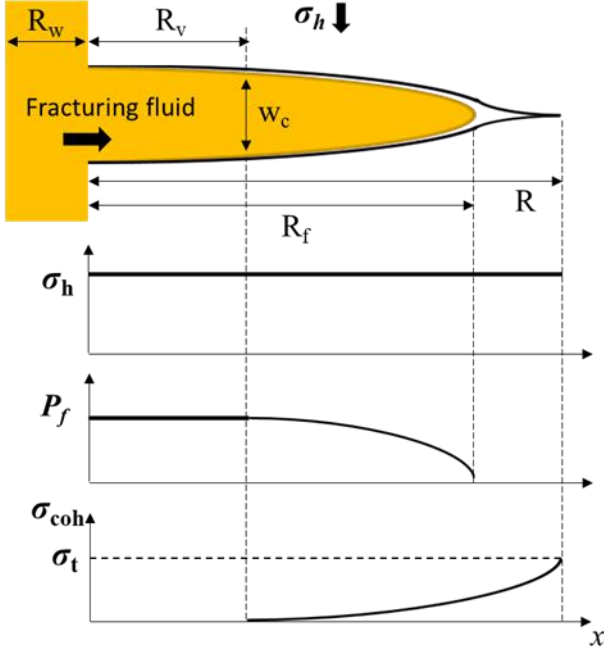


**Fig.B1** Schematic of loading of a penny-shaped hydraulic fracture with fluid lag (Image modified from Lhomme (2005))

The summation of the three contributions (**Eqs.B1 to 3**) to the stress intensity factor ( $K_{HF}$ ) for hydraulic fracture is necessarily to be equal to zero at the true crack tip, reads:

$$K_{HF} = K_I(P_f) + K_I(\sigma_r) + K_I(\sigma_{coh}) = 0 \quad (\text{B6})$$

In order to propagate a hydraulic fracture, the  $K_{HF}$  must be larger than 0, reads:

$$2 \sqrt{\frac{R}{\pi}} \int_0^{c_f} K_{np}(\xi, c) p_f(\xi, t) d\xi > \left[ 2 \sqrt{\frac{R}{\pi}} \sigma_r \int_0^c K_{np}(\xi, c) d\xi + 2 \sqrt{\frac{R}{\pi}} \sigma_t \int_{c_v}^c K_{np}(\xi, c) f_{w_{ct}} d\xi \right] \quad (\text{B7})$$

and reduces to:

$$\int_0^{c_f} K_{np}(\xi, c) p_f(\xi, t) d\xi > \left[ \sigma_r \int_0^c K_{np}(\xi, c) d\xi + \sigma_t \int_{c_v}^c K_{np}(\xi, c) f_{w_{ct}} d\xi \right] \quad (\text{B8})$$

It can be seen that both  $\sigma_r$  and  $\sigma_{coh}$  provide the resistance for initiation and propagation of a hydraulic fracture (HF). It is worthy to note that the intermediate stress  $\sigma_H$  may play an important role in  $K_I(\sigma_r)$  if the HF is inclined to the directions of both horizontal stresses. Therefore, the performance of  $\sigma_H$  and the intermediate strain  $\varepsilon_H$  induced by HF propagation are worthily to be monitored/evaluated (see **Section 4.2**). The cohesive stress  $\sigma_{coh}$  profoundly affect the propagation of a HF, especially for soft/ductile materials under stress field (Ju et al. 2021; Liu and Lecampion 2021; Papanastasiou 1997; Papanastasiou and Thiercelin 1993). If the different materials exhibit the same value of both  $K_I(P_f)$  and  $K_I(\sigma_r)$ , the  $K_I(\sigma_{coh})$  will be the dominated parameter differentiating the behaviour of fracture propagation.

## Reference

- Aharonov E, Scholz CH (2019) The brittle-ductile transition predicted by a physics-based friction law. *Journal of Geophysical Research: Solid Earth* 124:2721-2737
- Amitrano D (2003) Brittle-ductile transition and associated seismicity: Experimental and numerical studies and relationship with the b value. *Journal of Geophysical Research: Solid Earth* 108
- Bakhshi E, Golsanami N, Chen L (2021) Numerical modeling and lattice method for characterizing hydraulic fracture propagation: a review of the numerical, experimental, and field studies. *Archives of Computational Methods in Engineering* 28:3329-3360
- Barenblatt GI (1962) The mathematical theory of equilibrium cracks in brittle fracture. *Advances in applied mechanics* 7:55-129
- Boone T, Wawrzynek P, Ingraffea A Simulation of the fracture process in rock with application to hydrofracturing. In: *International Journal of Rock Mechanics and Mining Sciences & Geomechanics Abstracts*, 1986. vol 3. Elsevier, pp 255-265
- Brantut N, Schubnel A, Guéguen Y (2011) Damage and rupture dynamics at the brittle-ductile transition: The case of gypsum. *Journal of Geophysical Research: Solid Earth* 116
- Bunger AP (2005) Near-surface hydraulic fracture. University of Minnesota,
- Desroches J, Detournay E, Lenoach B, Papanastasiou P, Pearson JRA, Thiercelin M, Cheng A (1994) The crack tip region in hydraulic fracturing. *Proceedings of the Royal Society of London Series A: Mathematical and Physical Sciences* 447:39-48
- Dugdale DS (1960) Yielding of steel sheets containing slits. *Journal of the Mechanics and Physics of Solids* 8:100-104
- Economides MJ, Nolte KG (1989) *Reservoir stimulation vol 2*. Prentice Hall Englewood Cliffs, NJ,
- Elices M, Guinea G, Gomez J, Planas J (2002) The cohesive zone model: advantages, limitations and challenges. *Engineering fracture mechanics* 69:137-163
- Evans B, Fredrich JT, Wong TF (1990) The brittle-ductile transition in rocks: Recent experimental and theoretical progress. *The Brittle-Ductile Transition in Rocks*, *Geophys Monogr Ser* 56:1-20
- Feng R, Zhang Y, Rezagholilou A, Roshan H, Sarmadivaleh M (2020) Brittleness Index: from conventional to hydraulic fracturing energy model. *Rock Mechanics and Rock Engineering* 53:739-753
- Feng R., Sarout J., Daustriat J., Ghuwainim Y., Rezaee R., Sarmadivaleh M (2022). Laboratory validation of a new hydro-mechanical energy-based brittleness index model for hydraulic fracturing. *EarthArXiv preprint*, DOI: [doi.org/10.31223/X55M1J](https://doi.org/10.31223/X55M1J)



- Garagash DI (2019) Cohesive-zone effects in hydraulic fracture propagation. *Journal of the Mechanics and Physics of Solids* 133:103727
- Gischig VS, Preisig G Hydro-fracturing versus hydro-shearing: a critical assessment of two distinct reservoir stimulation mechanisms. In: 13th ISRM International Congress of Rock Mechanics, 2015. OnePetro,
- Hillerborg A, Modéer M, Petersson P-E (1976) Analysis of crack formation and crack growth in concrete by means of fracture mechanics and finite elements. *Cement and concrete research* 6:773-781
- Huang C, Chen S (2021) Effects of Ductility of Organic-Rich Shale on Hydraulic Fracturing: A Fully Coupled Extended-Finite-Element-Method Analysis Using a Modified Cohesive Zone Model. *SPE Journal* 26:591-609
- Huang K, Ghassemi A A coupled nonlocal damage model for hydraulic fracture propagation. In: 50th US Rock Mechanics/Geomechanics Symposium, 2016. OnePetro,
- Irwin GR (1957) Analysis of stresses and strains near the end of a crack traversing a plate
- Ju Y, Wu G, Wang Y, Liu P, Yang Y (2021) 3D Numerical Model for Hydraulic Fracture Propagation in Tight Ductile Reservoirs, Considering Multiple Influencing Factors via the Entropy Weight Method. *SPE Journal*:1-18
- Keer L, Luk V, Freedman J (1977) Circumferential edge crack in a cylindrical cavity
- Lhomme T (2005) Initiation of hydraulic fractures in natural sandstones
- Li JX, Rezaee R, Müller TM (2020) Wettability effect on wave propagation in saturated porous medium. *The Journal of the Acoustical Society of America* 147:911-920
- Liu D, Brantut N (2022) Micromechanical controls on the brittle-plastic transition in rocks. arXiv preprint arXiv:221111831
- Liu D, Lecampion B (2021) Propagation of a plane-strain hydraulic fracture accounting for a rough cohesive zone. *Journal of the Mechanics and Physics of Solids* 149:104322
- Liu S., Klaus T., Feng R., Bona A., Sarmadivaleh M (2022). Microstructure-based Modelling of Hydraulic Fracturing in Low-Permeability Rocks using the Cohesive Element Method. *Engineering Fracture Mechanics*, 108912.
- Liu Y et al. (2020) Mechanical properties and failure behavior of dry and water-saturated anisotropic coal under true-triaxial loading conditions. *Rock Mechanics and Rock Engineering* 53:4799-4818
- Mandal PP, Sarout J, Rezaee R (2020) Geomechanical appraisal and prospectivity analysis of the Goldwyer shale accounting for stress variation and formation anisotropy. *International Journal of Rock Mechanics and Mining Sciences* 135:104513
- Minaeian V (2014) True triaxial testing of sandstones and shales. Curtin University
- Nilson R, Proffer W (1984) Engineering formulas for fractures emanating from cylindrical and spherical holes
- Nygård R, Gutierrez M, Bratli RK, Høeg K (2006) Brittle–ductile transition, shear failure and leakage in shales and mudrocks. *Marine and Petroleum Geology* 23:201-212
- Papanastasiou P (1997) The influence of plasticity in hydraulic fracturing. *International Journal of Fracture* 84:61-79
- Papanastasiou P, Thiercelin M Influence of inelastic rock behaviour in hydraulic fracturing. In: *International journal of rock mechanics and mining sciences & geomechanics abstracts*, 1993. vol 7. Elsevier, pp 1241-1247
- Parisio F et al. (2021) A laboratory study of hydraulic fracturing at the brittle-ductile transition. *Scientific Reports* 11:1-16
- Rahjoo M, Eberhardt E (2021) Development of a 3-D confinement-dependent dilation model for brittle rocks; Part 1, derivation of a Cartesian plastic strain increments ratios approach for non-potential flow rules. *International Journal of Rock Mechanics and Mining Sciences* 145:104668

- Ramos Gurjao KG, Gildin E, Gibson R, Everett M (2022) Investigation of Strain Fields Generated by Hydraulic Fracturing with Analytical and Numerical Modeling of Fiber Optic Response. *SPE Reservoir Evaluation & Engineering* 25:367-379
- Richard D, Lerner E, Bouchbinder E (2021) Brittle to ductile transitions in glasses: Roles of soft defects and loading geometry. arXiv preprint arXiv:210305258
- Sarmadivaleh M (2012) Experimental and numerical study of interaction of a pre-existing natural interface and an induced hydraulic fracture. Curtin University
- Sarmadivaleh M, Rasouli V (2015) Test design and sample preparation procedure for experimental investigation of hydraulic fracturing interaction modes. *Rock Mechanics and Rock Engineering* 48:93-105
- Sarvaramini E, Dusseault MB, Komijani M, Gracie R (2019) A non-local plasticity model of stimulated volume evolution during hydraulic fracturing. *International Journal of Solids and Structures* 159:111-125
- Schmidt P, Dutler N, Steeb H (2022) Importance of fracture deformation throughout hydraulic testing under in situ conditions. *Geophysical Journal International* 228:493-509
- Tan Y, Wang S, Rijken M, Hughes K, Ning ILC, Zhang Z, Fang Z (2021) Geomechanical Template for Distributed Acoustic Sensing Strain Patterns during Hydraulic Fracturing. *SPE Journal* 26:627-638
- Vachaparampil A, Ghassemi A (2017) Failure characteristics of three shales under true-triaxial compression. *International Journal of Rock Mechanics and Mining Sciences* 100:151-159
- Van Dam D, De Pater C Roughness of hydraulic fractures: The importance of in-situ stress and tip processes. In: *SPE Annual Technical Conference and Exhibition, 1999*. OnePetro,
- Van Dam D, De Pater C, Romijn R (2000) Analysis of hydraulic fracture closure in laboratory experiments. *SPE Production & Facilities* 15:151-158
- Vinci C, Renner J, Steeb H (2014) A hybrid-dimensional approach for an efficient numerical modeling of the hydro-mechanics of fractures. *Water Resources Research* 50:1616-1635
- Wang H (2019) Hydraulic fracture propagation in naturally fractured reservoirs: Complex fracture or fracture networks. *Journal of Natural Gas Science and Engineering* 68:102911
- Wang S, Sloan S, Fityus S, Griffiths D, Tang C (2013) Numerical modeling of pore pressure influence on fracture evolution in brittle heterogeneous rocks. *Rock mechanics and rock engineering* 46:1165-1182
- Weinberg RF, Regenauer-Lieb K (2010) Ductile fractures and magma migration from source. *Geology* 38:363-366
- Wong T-f, Baud P (2012) The brittle-ductile transition in porous rock: A review. *Journal of Structural Geology* 44:25-53
- Wrobel M, Papanastasiou P, Dutko M (2022) On the pressure decline analysis for hydraulic fractures in elasto-plastic materials. arXiv preprint arXiv:220206581
- Wu R (2006) Some fundamental mechanisms of hydraulic fracturing. Georgia Institute of Technology,
- Yang Y, Liu S, Chang X (2021) Fracture stiffness evaluation with waterless cryogenic treatment and its implication in fluid flowability of treated coals. *International Journal of Rock Mechanics and Mining Sciences* 142:104727
- Yu B, Liu C, Chen W, Lu J, Liu Y (2022) Experimental study on deformation and fracture characteristics of coal under different true triaxial hydraulic fracture schemes. *Journal of Petroleum Science and Engineering* 216:110839

This is a non-peer reviewed EarthArXiv preprint.

- Zeng L, Reid N, Lu Y, Hossain MM, Saeedi A, Xie Q (2020) Effect of the fluid–shale interaction on salinity: implications for high-salinity flowback water during hydraulic fracturing in shales. *Energy & Fuels* 34:3031-3040
- Zhang J, Davis DM, Wong T-F (1993) The brittle-ductile transition in porous sedimentary rocks: Geological implications for accretionary wedge aseismicity. *Journal of Structural Geology* 15:819-830
- Zhang X, Jeffrey RG, Thiercelin M (2009) Mechanics of fluid-driven fracture growth in naturally fractured reservoirs with simple network geometries. *Journal of Geophysical Research: Solid Earth* 114
- Zhang Z et al. (2020) Modeling of fiber-optic strain responses to hydraulic fracturing. *Geophysics* 85:A45-A50
- Zhou J, Chen M, Jin Y, Zhang G-q (2008) Analysis of fracture propagation behavior and fracture geometry using a tri-axial fracturing system in naturally fractured reservoirs. *International Journal of Rock Mechanics and Mining Sciences* 45:1143-1152